International Journal of Heat and Mass Transfer 127 (2018) 526–534

Contents lists available at ScienceDirect

International Journal of Heat and Mass Transfer

journal homepage: www.elsevier.com/locate/ijhmt

Thermal characteristics of silicon wafer-based TVCs (thin vapor chambers) with disk-shape using DI water

Soo Bin Kim [a], Kyu Han Kim [a], Seok Pil Jang [a,b,*], M.A. Kedzierski [b]

[a] School of Aerospace and Mechanical Engineering, Korea Aerospace University, Goyang, Gyeonggi-do 412-791, Republic of Korea
[b] National Institute of Standards and Technology, Bldg. 226, Rm B 114, Gaithersburg, MD 20899, USA

ARTICLE INFO

Article history:
Received 2 May 2018
Received in revised form 18 June 2018
Accepted 19 June 2018
Available online 14 July 2018

Keywords:
Thin vapor chambers (TVCs)
Maximum heat transfer rate
Thermal resistance model
Laser heat source
IR camera

ABSTRACT

This paper analytically and experimentally investigates the thermal characteristics of disk-shaped, silicon wafer-based thin vapor chamber (TVC) using de-ionized water as the working fluid. The maximum heat transfer rate, the maximum temperature, and the thermal resistances of the TVCs were measured experimentally. An analytical model based on the modified liquid pressure drop through a micro-pin–fin wick and the capillary limit was developed to determine the maximum heat transfer rate. In addition, a thermal resistance model was developed for the TVC that was used to calculate the maximum temperature from the maximum heat transfer rate. The maximum temperature of TVCs is ensured to not exceed the maximum allowable temperature of the electronic components. The silicon wafer-based TVCs, which have an overall thickness of 1 mm and radii of 5 mm, 7.5 mm, and 10 mm, were manufactured by using both deep reactive ion etching (DRIE) and Ionic bonding. A laser heat source and an IR camera were used not only to eliminate the effect of a thermal contact resistance between the heat source and the TVCs, but they were also used to observe the burn-out phenomena in the TVCs directly. The analytical model was shown to predict most of the measured data within ±10%. The effect that key TVC design parameters, such as the TVCs' radius, the fin diameter, and the wick height, had on its maximum temperature and its thermal resistance were illustrated with the model and the measurements.

1. Introduction

Mobile devices such as smartphones and various kinds of tablets having communication, video, audio, and game functions, have massive heat dissipation due to the compactness of the application processor (AP) [1]. Providing thermal designs that meet the high heat dissipation rates associated with mobile devices have been a challenge for some time [1,2]. One successful approach that has been used to meet the high-performance cooling requirements, while using the surroundings as a heat sink, is thin vapor chambers (TVCs) [2–6]. However, a few design and measurement hurdles must be overcome before TVCs can be ensured to meet the cooling requirements of the newest mobile devices. The first is that the vapor chamber needs to be very thin (less than 1 mm) [2,7,8] while maintaining dimensional integrity during operation while the internal pressure increases. This may cause a problem of bulging and bending of thin-metal-walled (<1 mm) TVCs when internal pressures exceed design limits. The second problem is that measurement techniques that rely on film heaters can potentially introduce large measurement errors due to the thermal contact resistance between the film heater and the surface of the TVCs. Despite this, many investigations do not consider the contact thermal resistance [9–11]. In addition, it is important to be able to predict and to measure the maximum temperature of a TVC so that it can be maintained below the allowable temperature of electronic components in the mobile device. Moreover, the maximum heat transfer rate of the TVCs should be calculated by considering both the capillary limit and the allowable maximum temperature of electronic components in the mobile device. However, many researchers experimentally or numerically present only the maximum heat transfer rate [12,13] without regard to the allowable maximum temperature of the electronic components in the mobile device.

The main objective of this study was to analytically and experimentally investigate the thermal characteristics of disk-shaped, silicon wafer-based TVCs. An analytical solution for the maximum heat transfer rate was obtained by considering the capillary limit and the modified liquid pressure drop through the micro-pin-fin wick structure to predict the point where the wick runs dry. A theoretical model for thermal resistance of TVCs was also developed,

* Corresponding author at: School of Aerospace and Mechanical Engineering, Korea Aerospace University, Goyang, Gyeonggi-do 412-791, Republic of Korea.
E-mail address: spjang@kau.ac.kr (S.P. Jang).

https://doi.org/10.1016/j.ijheatmasstransfer.2018.06.100
0017-9310/

Nomenclature

A	area [m^2]
d_f	fin diameter [m]
h	height of vapor core [m]
h_c	wall thickness of TVCs [m]
h_{fg}	latent enthalpy of the working fluids [kJ kg^{-1}]
$h_{m,c}$	average height of liquid captured by wick structure at the condenser [m]
$h_{m,e}$	average height of liquid captured by wick structure at the evaporator [m]
h_w	height of the wick [m]
$\bar{h}_{film}$	film heat transfer coefficient [W m^{-1} K^{-1}]
k_l	thermal conductivity of the working fluid as liquid phase [W m^{-2} K^{-1}]
K	permeability [m^2]
n	number of pin-fins at evaporator
p	pressure [Pa]
Q_{max}	maximum heat transfer rate [W]
r	radius coordinate
$r_{c,min}$	minimum capillary radius of pin-fin wick structure [m]
R	overall radius of a TVC [m]
R_e	radius of evaporator region at a TVC [m]
R_{th}	thermal resistance [K W^{-1}]
Re_h	Reynolds number based on height of vapor core [–]
s	shortest distance between pin-fins [m]
T	temperature [K]
u_l	liquid velocity [m s^{-1}]
v_1	vapor injection velocity at evaporator [m s^{-1}]

Greek symbols

δ	liquid film thickness [m]
ε	porosity [–]
σ	surface tension [N m^{-1}]
μ	viscosity [Pa s]
ν	kinematic viscosity [m^2 s^{-1}]
ρ	density [m^3 kg^{-3}]
θ	contact angle [radians]
φ	square root of the ratio of the evaporator area to the TVC's surface area [–]

Subscript

b	bottom
c	condenser
e	evaporator
l	liquid
max	maximum
t	top
v	vapor
w	wick

Superscript

+	dimensionless quantities

which was used along with the maximum heat transfer to predict the maximum temperature of TVCs. The maximum allowable temperature limit is defined as the maximum temperature permitted for normal operation of electronic components. If the maximum temperature as calculated from the models exceeds the maximum allowable temperature, then the reported maximum heat transfer rate of TVCs was reduced to match that which is associated with the maximum allowable temperature. The dominant factors which strongly affect the thermal characteristics of the TVCs were analytically identified. For silicon wafer-based TVCs, the deep reactive ion etching (DRIE) and Ionic bonding manufacturing process eliminates the effects of bulging and bending due to overpressure. The measurements showed that the key parameters affecting the maximum temperature and the thermal resistances of the silicon wafer-based TVCs were the overall radius, the pin-fin diameter, and the wick height. A laser was used as a heat source to eliminate the effect of contact thermal resistance that would have occurred with an attached film heater. In addition, the burn-out phenomenon was noninvasively and directly observed with an IR camera. The predictions from analytical models were mainly within ±10% of the experimental results. Finally, the analytical and experimental effect of varying key engineering parameters, such as the overall radius of the TVC, the fin diameter and the height of the micro-pin-fin in the wick structure, on the maximum temperature and the thermal resistance are presented.

2. Theoretical approaches

Fig. 1 shows a schematic of the governing heat transfer mechanisms, which are basically those of a heat pipe, and the overall structure of the TVC that is analyzed in this study. The schematic shows the evaporator region where the chip to be cooled is fixed. The heat that is produced by the chip is removed by the evaporation of the fluid retained in the wick structure of TVCs by surface-tension forces. The vapor generated by the evaporator is condensed onto the condenser region as shown in Fig. 1.

2.1. Analytical model of maximum heat transfer rate of TVCs at the capillary limit

Vafai et al. [13] have developed one of the first analytical solutions for the vapor phase and the liquid phase velocity and pressure distributions for disk-shaped heat pipes which were similar to the overall geometry shown in Fig. 1. The maximum heat transfer rate was governed by the surface-tension driven flow pressure distribution as described by the Young-Laplace equation. Recently Kim et al. [14] modified the boundary condition and corrected several typos in the Vafai et al. [13] solution to analytically obtain the pressure drop. The vapor pressure distribution presented by Kim et al. [14] and used in this paper is:

$$p_v^+(r^+) = \begin{cases} [0 \leqslant r^+ \leqslant \varphi R^+] \\ p_v^+(0) - \frac{24}{25}\left\{\frac{(1-\varphi^2)}{(2-\varphi^2)} Re_h R^+\right\}^2 \left(\frac{r^+}{R^+}\right)^2 \\ [\varphi R^+ \leqslant r^+ \leqslant R^+] \\ p_v^+(0) - \frac{8}{25}\left\{\frac{\varphi^2}{2-\varphi^2} Re_h R^+\right\}^2 \\ \times\left[3\left(\frac{r^+}{R^+}\right)^2 + \left(\frac{R^+}{r^+}\right)^2 - 4\ln\frac{r^+}{R^+} - 2\left(3 - 2\ln\varphi - \frac{1}{\varphi^2}\right)\right] \end{cases} \quad (1)$$

The nondimensional parameters are:

$$p_v^+ = \frac{p_v}{\rho_v v_1^2},\ r^+ = \frac{r v_v}{h^2 v_1},\ R^+ = \frac{R v_v}{h^2 v_1},\ Re_h = \frac{v_1 h}{v_v},\ \varphi^2 = \frac{A_e}{\pi R^2} \quad (2)$$

where $A_e, h, p_v, p_v^+, r, r^+, R, R^+, Re_h, v_1, v_v, \rho_l, \rho_v$ and φ respectively are the evaporator area, the height of vapor core, the vapor pressure, the dimensionless vapor pressure, the radial coordinate, the dimensionless radial coordinate, the overall radius of the TVC, the dimensionless radius of the TVC, the Reynolds number, the vapor injection

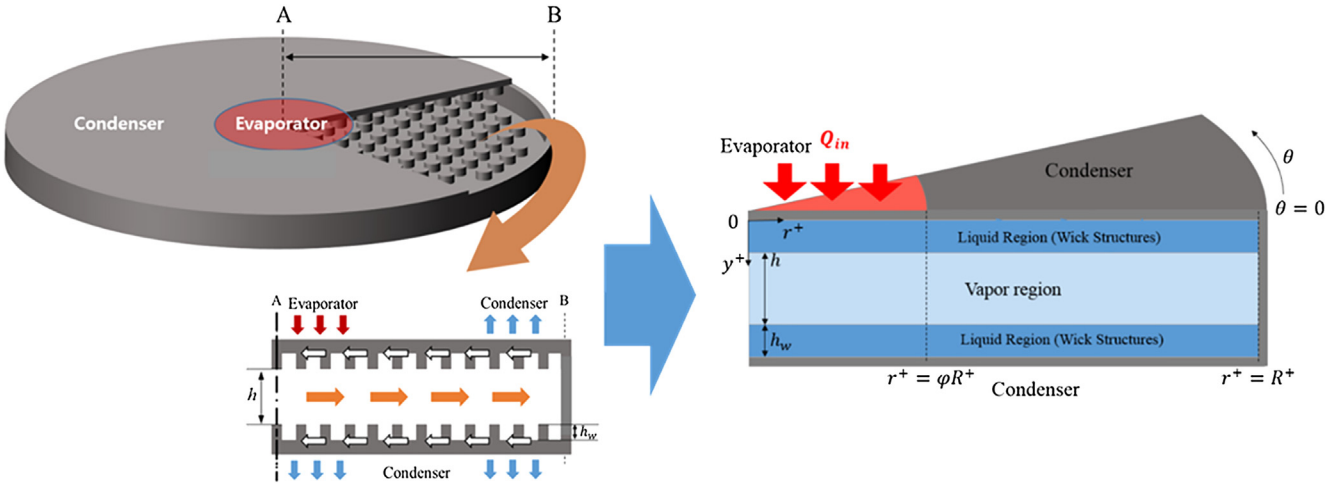

Fig. 1. Schematic view of a silicon-based TVC with pin-fin wick structure.

velocity at the evaporator ($0 \leqslant r^+ \leqslant \varphi R^+$), the kinematic viscosity of vapor, the liquid density, the vapor density, and the square root of the ratio of the evaporator area to the surface area of the TVC.

Vafai et al. [13] also provide an analytical solution for the liquid pressure distribution through the wick by using the Darcy equation, which does not account for the no-slip condition at the wall. Considering that the maximum heat transfer strongly depends on the liquid pressure drop through the micro-pin-fin wick, the Vafai et al. [13] solution was modified to account for the no-slip condition with the use of the Brinkman-Darcy equation:

$$\frac{dP_l^+}{dr^+} = \frac{u_l^+}{K^+}\frac{v^+}{(h_w^+)^2} - \frac{\varepsilon v^+}{Re_h^2}\left(\frac{1}{r^+}\frac{\partial u_l^+}{\partial r^+} + \frac{\partial^2 u_l^+}{\partial r^{+2}} + \frac{\partial^2 u_l^+}{\partial y^{+2}}\right) \tag{3}$$

The nondimensional parameters are:

$$p_l^+ = \frac{p_l}{\rho_l v_1^2},\ u_l^+ = \frac{u_l}{v_1},\ v^+ = \frac{v_l}{v_v},\ K^+ = \frac{K}{h_w},\ h_w^+ = \frac{h_w}{h},\ y^+ = \frac{y}{h} \tag{4}$$

where $h_w, h_w^+, K, K^+, p_l, p_l^+, u_l, u_l^+, y, y^+, \varepsilon, v_l$ and v^+ respectively are the height of the wick, the dimensionless height of the wick, the permeability, the dimensionless permeability, the liquid pressure, the dimensionless liquid pressure, the liquid velocity, the dimensionless liquid velocity, the y- coordinate, the dimensionless y- coordinate, porosity, the kinematic viscosity of liquid, and the dimensionless kinematic viscosity. The permeability (K) and the porosity (ε) of the micro-pin-fin wick structure is given by Kavinary [15]:

$$K = 0.0606 d_f^2 \frac{\pi}{4}\frac{\varepsilon^{5.1}}{1-\varepsilon} \text{ and } \varepsilon = \frac{V_{pore}}{V_{total}} = \frac{(s+d_f)^2 - \pi(d_f/2)^2}{(s+d_f)^2} \tag{5}$$

where d_f and s are the fin diameter and the shortest distance among pin-fins, respectively. The requirement that the pressure profiles be continuous at $r = R^+$, i.e., the vapor and liquid pressures are equal at $r = R^+$, can be written in dimensionless form as:

$$p_1^+(R^+) = \left(\frac{1}{\rho^+}\right)p_v^+(R^+), \tag{6}$$

Mass continuity for the region with the evaporator ($0 \leqslant r^+ \leqslant \varphi R^+$) and the region with only condensers ($\varphi R^+ \leqslant r^+ \leqslant R^+$) can be written as:

$$\begin{aligned} &\frac{2}{r^+}\frac{\partial}{\partial r^+}(r^+ u_l^+) + \frac{1}{\rho^+}\frac{v_2^+ - v_1^+}{dy^+} = 0 \quad (0 \leqslant r^+ \leqslant \varphi R^+) \\ &\frac{\partial}{\partial r^+}(u_l^+) + \frac{u_l^+}{r^+} + \frac{1}{\rho^+}\frac{v_2^+}{h_w^+} = 0 \quad (\varphi R^+ \leqslant r^+ \leqslant R^+) \end{aligned} \tag{7}$$

Integration of Eq. (7) with respect to y^+ and r^+ yields the dimensionless liquid velocity at each region:

$$\begin{aligned} u_l^+ &= \frac{v_1^+ - v_2^+}{4\rho^+ h_w^+} r^+ \quad (0 \leqslant r^+ \leqslant \varphi R^+) \\ u_l^+ &= -\frac{v_2^+}{2\rho^+ h_w^+}\frac{(r^+)^2 - (R^+)^2}{r^+} \quad (\varphi R^+ \leqslant r^+ \leqslant R^+) \end{aligned} \tag{8}$$

Substitution of Eq. (8) into the governing equation, i.e., Eq. (2) and integrating, results in the dimensionless liquid pressure distribution through the wick:

$$p_l^+(r^+) = \begin{cases} [0 \leqslant r^+ \leqslant \varphi R^+] \\ p_v^+(R^+) + \frac{v^+}{4\rho^+ K^+ (h_w^+)^3}\frac{\varphi^2 Re_h}{(2-\varphi^2)}\left[\frac{1-\varphi^2}{\varphi^2}(r^+)^2 + 2(R^+)^2\ln(\varphi)\right] \\ + \frac{v^+}{4\rho^+ h_w^+}\frac{\varphi^2\varepsilon}{(2-\varphi^2)Re_h}\left[\frac{1-\varphi^2}{\varphi^2}\left\{1 - 2\ln\left(\frac{\varphi R^+}{r^+}\right)\right\} + 2\ln\left(\frac{1}{\varphi}\right)\right] \\ [\varphi R^+ \leqslant r^+ \leqslant 1] \\ p_v^+(R^+) + \frac{v^+}{4\rho^+ K^+ (h_w^+)^3}\frac{\varphi^2 Re_h}{(2-\varphi^2)}\left[(R^+)^2 - (r^+)^2 - 2(R^+)^2\ln\left(\frac{R^+}{r^+}\right)\right] \\ + \frac{v^+}{4\rho^+ h_w^+}\frac{\varphi^2\varepsilon}{(2-\varphi^2)Re_h}\left[\frac{(R^+)^2-(r^+)^2}{(r^+)^2} + 2\ln\left(\frac{R^+}{r^+}\right)\right] \end{cases} \tag{9}$$

$$\rho^+ = \frac{\rho_l}{\rho_v} \tag{10}$$

where ρ^+ is dimensionless density. Eqs. (1) and (9) were used to calculate the maximum heat transfer rate of the vapor chamber analytically, while using the Young-Laplace equation at $r = 0$ (capillary limit) [13,16] as:

$$P_v(0) - P_l(0) = \frac{2\sigma}{r_{c,min}(0)} \tag{11}$$

where $r_{c,min}$ and σ are the minimum capillary radius of pin-fin wick structure and the surface tension, respectively. The minimum capillary radius of pin-fin wick structure is given by:

$$r_{c,min}(0) = \frac{4\cos\theta}{s} \tag{12}$$

where s and θ are the distance between pin-fins, and the contact angle, respectively. Eq. (11) can be rearranged using dimensionless parameters as:

$$P_v^+(0) - \rho^+ P_l^+(0) = \frac{2}{s^+}\frac{1}{Re_h^2}\cos\theta, \quad s^+ = \frac{s\rho_v v_v^2}{\sigma h^2} \tag{13}$$

where s^+ is the dimensionless smallest distance between pin-fins. Substituting Eqs. (1) and (9) into Eq. (13), the equation can be rearranged using the Reynolds number, Re_h to obtain the maximum heat transfer rate Q_{max}:

$$Q_{max} = \frac{\mu_v A_e h_{fg}}{h}\left(\frac{-B+\sqrt{B^2-4AC}}{2A}\right) \tag{14}$$

$$A = \left(\frac{4}{5}\frac{\varphi^2}{2-\varphi^2}\right)^2\left\{2\ln\varphi + \frac{(5\varphi^2-3)(\varphi^2-7)}{16\varphi^2} + \frac{3}{4}\right\}\frac{1}{(h^+)^2}$$
$$B = -\left\{\frac{v^+}{2}\frac{\varphi^2}{2-\varphi^2}\ln\varphi\right\}\frac{1}{K^+(h_w^+)^3(h^+)^2} \tag{15}$$
$$C = -\frac{2}{s^+}\cos\theta$$

where h_{fg}, Q_{max} and μ_v are the latent enthalpy of the working fluids, the maximum heat transfer rate at the capillary limit, and the viscosity of vapor, respectively. The contact angle between the silicon wafer and the water has been typically reported as between 45° and 50° [17]. However, this value does not account for the effect of roughness. In order to account for the surface roughness of the DRIE produced surface, a contact angle of 85° between the etched silicon and DI water was used in analytical model [18]. In addition, a surface tension of 6.78×10^{-2} N m^{-1} [19] was used for the water.

2.2. Thermal resistance model and maximum temperature of TVCs

The thermal resistance model, which consists of three parts as shown in Fig. 2(a), is developed in this section. The first step was to model the thermal resistance of the evaporator region, and the second step was to model the thermal resistance of the vapor core in the TVC. The final step was to model the thermal resistances of the condenser region. The thermal resistances can be combined to obtain the complete model for the TVC as:

$$R_{th,total} = R_{th,evap} + \left[\frac{1}{R_{th,cond\_bottom}} + \frac{1}{R_{th,vapor\_core} + (1/R_{th,cond\_top} + 1/R_{th,cond-bottom})^{-1}}\right]^{-1} \tag{16}$$

where $R_{th,cond-bottom}$, $R_{th,cond-up}$, $R_{th,evap}$, $R_{th,vapor\_core}$, and $R_{th,total}$ are the thermal resistances of the condenser region at the bottom surface, the condenser region at the top surface, the evaporator region, the vapor core region, and the total thermal resistance, respectively. The thermal resistance of the vapor core region was neglected because it generally is much smaller than other thermal resistances [20]. In order to develop each thermal resistance model, the representative elementary volume of the micro-pin-fin wick structure at evaporator and condensor regions is shown in Fig. 2(b and c).

At the evaporator region, the thermal resistance can be modeled as:

$$R_{th,evap} = \left[\frac{1}{R_1+R_2+R_3} + \frac{1}{R_4+R_5}\right]^{-1} \tag{17}$$

$$R_1 = \frac{h_c}{k_s A_1},\ R_2 = \frac{h_{m,e}}{k_s A_1},\ R_3 = \frac{1}{\bar{h}_{film} A_2},\ R_4 = \frac{h_c}{k_s A_3},\ R_5 = \frac{h_{m,e}}{k_l A_3} \tag{18}$$

$$A_1 = \pi(R_e)^2(1-\varepsilon),\ A_2 = \pi d_f(h_w - h_{m,e})n,\ A_3 = \pi(R_e)^2(\varepsilon),\ n = \frac{A_1}{\frac{\pi}{4}d_f^2} \tag{19}$$

where A_1, A_2, A_3, d_f, h_c, $h_{m,e}$, h_w, $\bar{h}_{film}$, n and R_e respectively are the cross-sectional area of pin-fin wick at the evaporator, the side-surface area of pin-fin wick at the evaporator, the liquid area at evaporator, the fin diameter, the wall thickness of the TVC, the average height of the liquid captured by the pin-fin wick structure at the evaporator, the height of the wick, the film heat transfer coefficient, the number of pin-fins at evaporator, and the radius of the evaporator region. Also, it was assumed that the average height of liquid captured by the pin-fin wick structure at the evaporator ($h_{m,e}$) was h_w/10. The film heat transfer coefficient at the evaporator used for the model was taken from Chi [21]:

$$\bar{h}_{film} = \frac{k_l}{0.185 d_f} \tag{20}$$

where k_l is the thermal conductivity of the working fluids as the liquid phase.

As shown in Fig. 2(c), the remaining thermal resistance models to be developed are for the condenser regions at the top and the

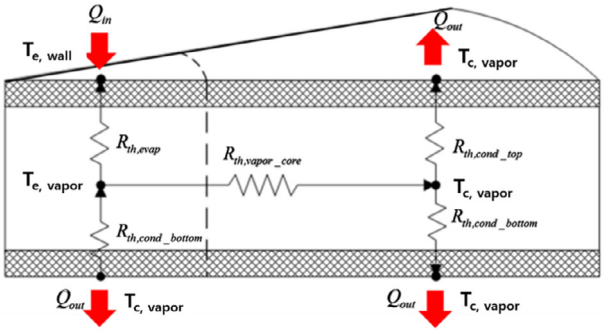

(a) Total thermal resistance model of a TVC

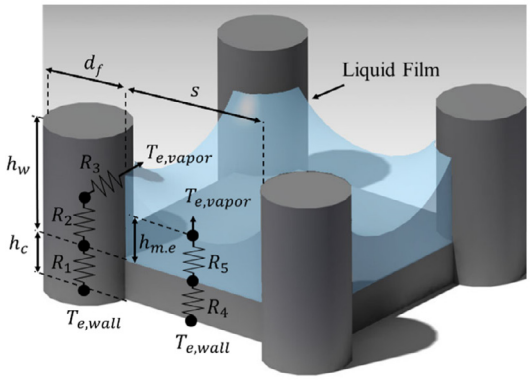

(b) Thermal resistance model at the evaporator

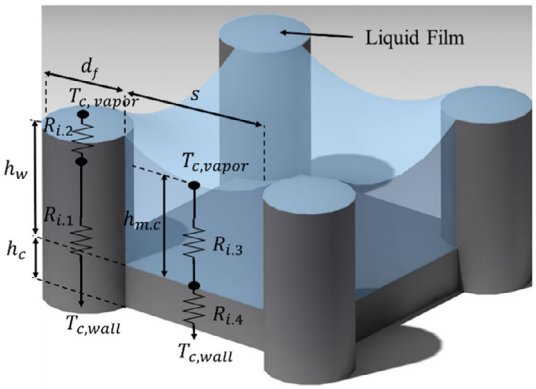

(c) Thermal resistance model at ith condenser ($i = t,\ b$)

Fig. 2. Total and partial thermal resistance models for a TVC.

bottom surface. The thermal resistance model at the condenser region of the top surface is given by:

$$R_{cond,top} = \left[\frac{1}{R_{t,1}+R_{t,2}} + \frac{1}{R_{t,3}+R_{t,4}}\right]^{-1} \tag{21}$$

$$R_{t,1} = \frac{h_c + h_w}{k_s A_4},\ R_{t,2} = \frac{\delta}{k_l A_4},\ R_{t,3} = \frac{h_{m,c}}{k_l A_5},\ R_{t,4} = \frac{h_c}{k_s A_5} \tag{22}$$

$$A_4 = \pi(R^2 - R_e^2)(1-\varepsilon),\ A_5 = \pi(R^2 - R_e^2)\varepsilon \tag{23}$$

where A_4, A_5, $h_{m,c}$ and δ respectively are the cross-sectional area of pin-fin wick at the condenser region of the top surface, the liquid

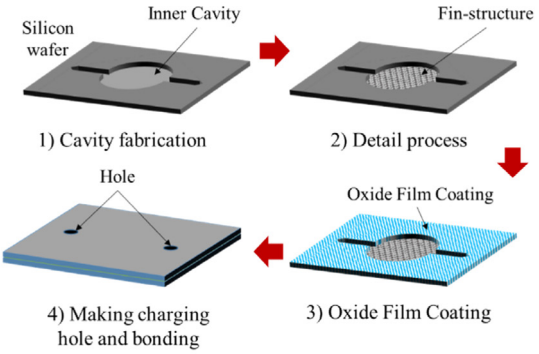

(a) Manufacturing processes

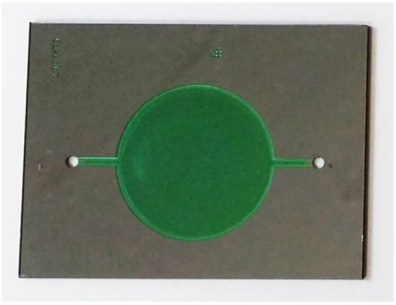

(b) Top view of TVC

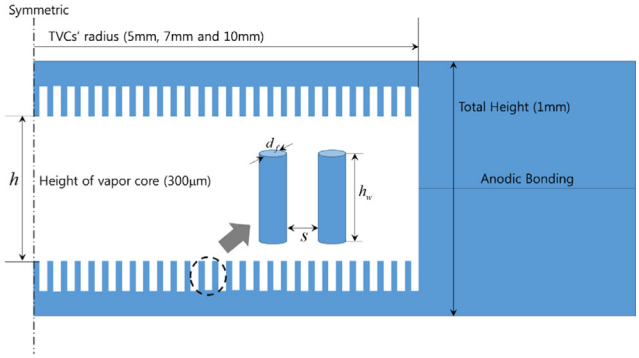

(c) Geometry of a TVC

Fig. 3. Silicon wafer-based TVC.

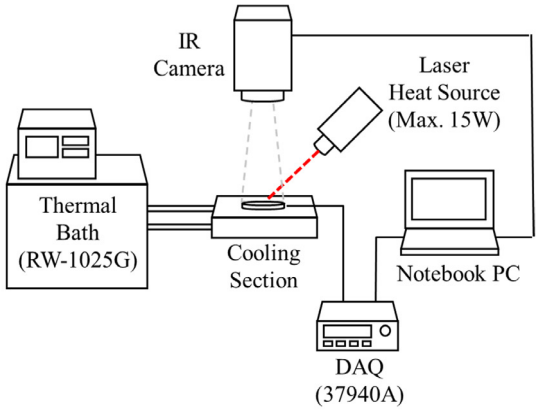

(a) Schematic of measurement system for temperature distribution of TVCs

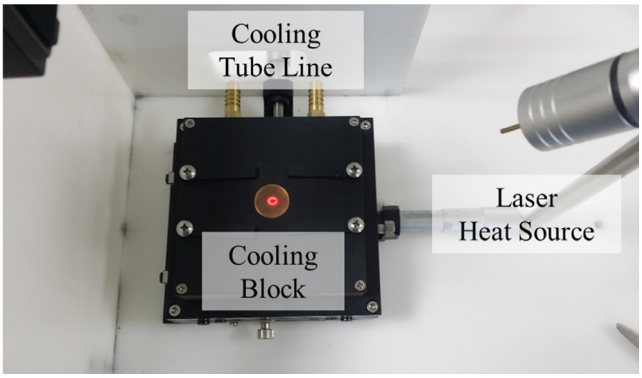

(b) Test section

Fig. 4. Photograph of measurement devices for thermal characteristics of TVCs.

Table 1
Geometry of fabricated TVCs.

Case	Radius (mm)	Fin diameter (μm)	Wick height (μm)	Vapor Core Thickness (μm)	Total Thickness (μm)
1	5	50	50	300	1000
2	7.5	50	50		
3	10	50	50		
4	10	150	50		
5	10	50	75		
6	10	50	100		

area at the condenser region of the top surface, the average height of the liquid captured by the pin-fin wick structure at the condenser and the liquid film thickness. In addition, it was assumed that $h_{m,c} = h_w$ [20], $\delta = 5$ μm and [22]. Also, the thermal resistance model at the condenser region of the bottom surface can be obtained by:

$$R_{cond,bottom} = \left[\frac{1}{R_{b,1} + R_{b,2}} + \frac{1}{R_{b,3} + R_{b,4}}\right]^{-1} \tag{24}$$

$$R_{b,1} = \frac{h_c + h_w}{k_s A_6},\ R_{b,2} = \frac{\delta}{k_l A_6},\ R_{b,3} = \frac{h_{m,c}}{k_l A_7},\ R_{b,4} = \frac{h_c}{k_s A_7} \tag{25}$$

$$A_6 = \pi R^2(1-\varepsilon),\ A_7 = \pi R^2 \varepsilon \tag{26}$$

where A_6 and A_7 are the cross-sectional area of the pin-fin wick at the condenser region of the bottom surface and the liquid area at the condenser region of the bottom surface, respectively.

2.3. Maximum heat transfer rate of TVCs at the capillary limit and allowable maximum temperature limit

With the thermal resistance model and the maximum heat transfer rate at the capillary limit, the maximum temperature can be obtained as:

$$T_{max} = \frac{Q_{max}}{R_{th,total}} + T_c \tag{27}$$

where T_{max} and T_c are the maximum temperature and the average temperature at the condensor region, respectively. It should be ensured that the maximum temperature of the TVC that is associated with the maximum heat transfer rate at the capillary limit does not exceed the allowable temperature limit of the electronic components. For the present study, the allowable maximum temperature limit is 70 °C. If the maximum temperature of the TVC at the maximum heat transfer (capillary limit) is larger than the allowable maximum temperature of the electronic components, then the maximum heat transfer rate of TVCs should be recalculated as:

$$Q_{max} = \frac{T_{AMTL} - T_c}{R_{th,total}} \tag{28}$$

where T_{AMTL} is the allowable maximum temperature which is 70 °C, respectively.

3. Experimental approach

3.1. Manufacturing processes of TVCs

The silicon-based TVCs with the pin-fin wick structure were fabricated following the processes shown in Fig. 3(a). To manufacture the TVCs with radii of 5 mm, 7.5 mm and 10 mm, and depth of 150 μm, two silicon wafers were etched using deep reactive ion etching (DRIE) [23]. To make pin-fin wick structure with wick heights of 50 μm, 75 μm, and 100 μm, and fin diameters of 50 μm and 150 μm, the inner surface of the cavity was also etched by DRIE. As shown in Fig. 3(a), two holes for charging working fluids were manufactured using laser machining at the bottom of the silicon wafer and the oxidation film was formed on the silicon surface before the two wafers were bonded together. The two silicon wafers were joined using anodic bonding.

To remove the non-condensable gas from the working fluids in the present study, the working fluid (DI water) was boiled in a pressure vessel and then dipped into liquid nitrogen to extract the non-condensable gas from working fluids. The fabricated TVCs were evacuated to 10^{-3} Pa to eliminate the non-condensable gas. After that, the TVCs were filled with working fluids to a volume of approximately of 140% of wick pore [24]. Six TVCs with DI water as the working fluid were manufactured for this study. Fig. 3(b) and Table 1 provides the detailed geometry for the fabricated TVCs.

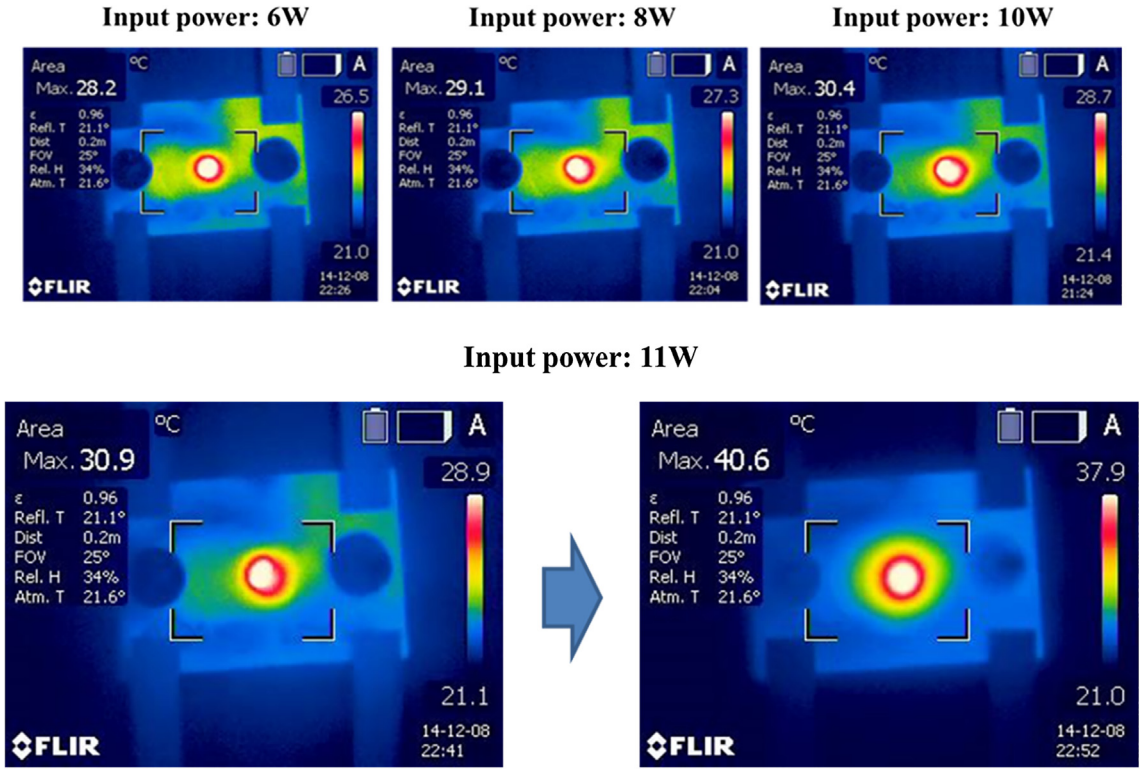

Fig. 5. Maximum heat transfer rate of case 4, TVC (TVC radius of 10 mm, fin diameter of 150 μm, wick fin height of 50 μm).

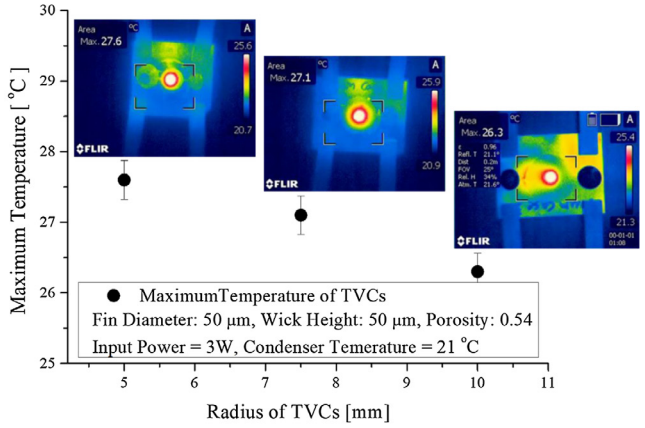

(a) Effect of the TVCs' radius on the maximum temperature

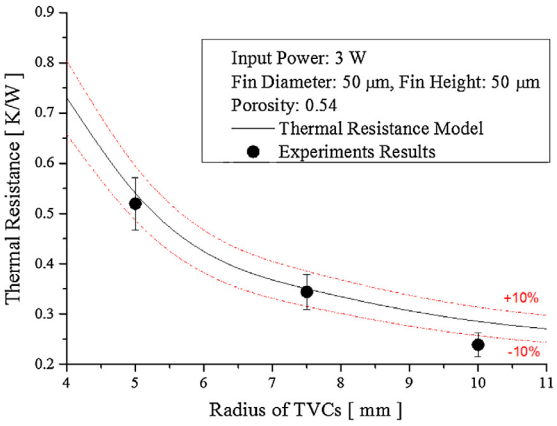

(b) Effect of the TVCs' radius on the thermal resistance

Fig. 6. The effect of the TVCs' radius on the thermal performance of TVCs.

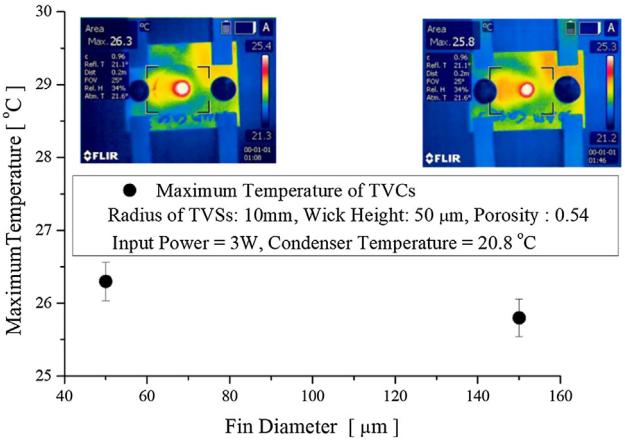

(a) Effect of the fin diameter on the maximum temperature

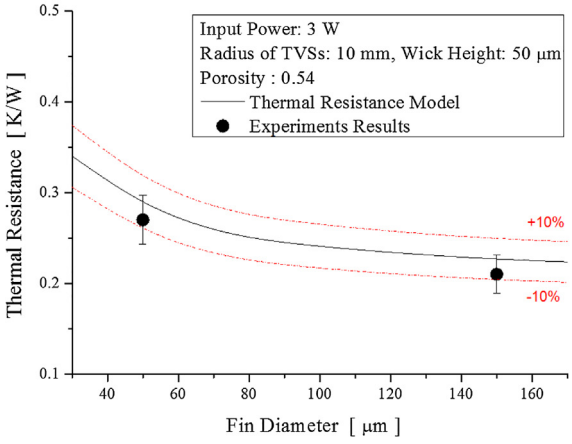

(b) Effect of the fin diameter on the thermal resistance

Fig. 7. The effect of the fin diameter on the thermal performance of TVCs.

With the six TVCs, the effects of TVCs' radius, the fin diameter, and the wick height on the maximum temperature and the thermal resistance were experimentally determined.

3.2. Experimental apparatus

Fig. 4 shows the experimental apparatus for measuring the temperature distribution on the TVCs and the maximum heat transfer rate. To minimize the contact thermal resistance between the evaporator and the surface of TVCs, a laser with maximum power of 15 W was used as the heat source. The maximum heat transfer rate and the surface temperature distributions were obtained using an IR (Infrared) camera. The benefit of the IR measurement is that it's a direct measurement of the working fluid temperature and it visually records the dry-out phenomenon through the IR-transparent silicon wafer [25]. These advantages make it possible to measure the maximum heat transfer rate of TVCs with IR. The emissivity of the IR camera was set to the emissivity of water (0.96). Also, the copper cooling block connected to the thermal bath was used to maintain the condenser region of TVCs at a low temperature.

To obtain the surface temperature distribution of TVCs, the temperature distribution of working fluids measured by IR camera is calibrated using 36-gauge T-type thermocouples which were attached to the surface. For the temperature range of 20–60 °C, the maximum uncertainty in the temperature calibration was approximately ±0.5 °C for a 95% confidence level and are shown as error bars on Figs. 6–8.

4. Results and discussions

4.1. Maximum heat transfer rate of TVCs

The maximum heat transfer rate of a disk-shaped TVC was predicted by the present analytical model (Eq. (28)) while considering a no-slip condition at the wall of the pin-fin wick structure for capillary limit and the maximum allowable temperature limit. Each of the test TVCs had a fixed evaporator region (5 mm diameter) regardless of the overall radius of the TVC. Measurements for the TVC for case 4 (radius of 10 mm, fin diameter of 150 μm, wick height of 50 μm, laser power up to 15 W) were used to validate the maximum heat transfer rate prediction. Fig. 5 shows that the TVC operates without dry-out up to an input power of 10 W. However, dry-out occurred in the TVC at a point between 10 W and 11 W, as evident by the temperature of the working fluid in the cavity dramatically increasing from 30.9 °C to 40.6 °C while the temperature distribution in the cavity was uniform for the 11 W condition. Dry-out is associated with all of the DI-water in the cavity being vaporized, resulting in pure conduction and a uniform surface temperature. Therefore, the best estimate of the maximum measured heat transfer rate, which occurs just prior to dry out, was approximately 10 W for case 4. This measurement is within approximately 6% of the prediction of 9.39 W for case 4. By using the

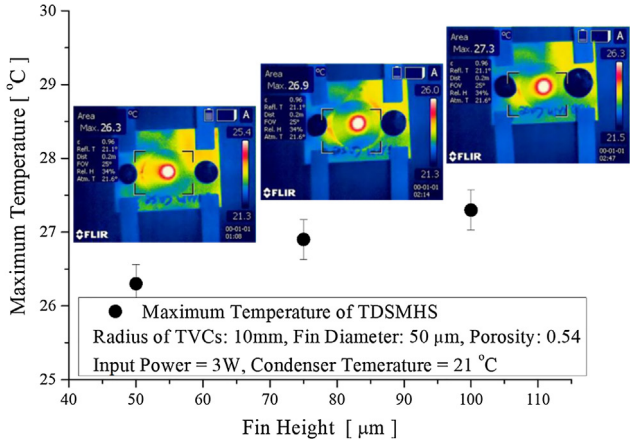

(a) Effect of the wick height on the maximum temperature

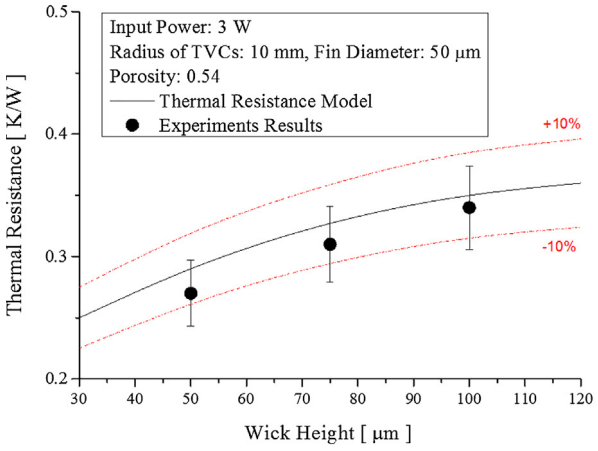

(b) Effect of the wick height on the thermal resistance

Fig. 8. The effect of the wick height on the thermal performance of TVCs.

last-observed, properly-operating TVC as the maximum performance prior to dry out, overall, the analytical model predicts the experimental data to within ±10%. The maximum heat transfer predicted by the analytical model for the manufactured TVCs are given in Table 2 at both the capillary limit and the allowable maximum temperature limit. As shown in Table 2, the maximum temperature at the maximum heat transfer rate is smaller than the allowable maximum temperature limit for all cases. Also, Table 3 shows theoretically results of the maximum heat transfer of TVC with optimized fin diameters and porosity for fixed h_w and h. Table 3 shows that the maximum temperature exceeds the maximum allowable temperature when the TVCs have a fin diameter larger than 50 μm with a wick height of 41.6 μm and a radius less than 5 mm. As a result, the maximum heat transfer rate for the TVCs was recalculated using Eq. (28) to ensure that the maximum allowable temperature of the electronic components was not exceeded.

4.2. Maximum temperature and thermal resistance of TVCs

4.2.1. Effect of TVC radius on the maximum temperature and the thermal resistance

TVCs for Case 1, 2 and 3 as shown in Table 1 are used to investigate the effect of the TVC radius on the maximum temperature and on the thermal resistance of the TVCs. The TVCs all have the same wick geometry (fin diameter = 50 μm, wick height = 50 μm) and the same input laser power of 3 W. As shown in Fig. 6(a), the maximum temperature is obtained from the temperature distribution on the surface as measured by the IR camera. The uncertainty for the thermal resistance was approximately ±10% for the 95% confidence level and are represented as error bars on Figs. 6–8. The maximum temperature decreases as the radius of the TVC increases. This shows that a larger condenser area plays an important role in reducing the total thermal resistance. As shown in Fig. 6(b), the analytical model of the thermal resistance is within ±10% of the experimental data. Fig. 6 shows that both the thermal resistance and the maximum temperature decrease as the radius of the TVC increases. Consequently, the radius of a TVC should be carefully designed to be large enough so that its temperature remains below the allowable maximum temperature of the electronic component and to ensure that the maximum heat transfer rate can be met.

4.2.2. Effect of fin diameter on the maximum temperature and the thermal resistance

Case 3 and Case 4 show the effect of the fin diameter on the maximum temperature and on the thermal resistance of TVCs. The TVCs both have a radius of 10 mm and a wick height of 50 μm, but have different fin diameters of 50 μm and 150 μm. The input power was fixed at 3 W. Fig. 7 (a) shows the maximum temperature as a function of the fin diameter of the wick structure.

Table 2
Predicted maximum heat transfer rate of the manufactured TVCs under both the capillary limit and the allowable maximum temperature limit (70 °C).

Case	Radius (mm)	d_f (μm)	ε	h_w (μm)	h (μm)	s (μm)	Q_{max} (W)	R_{th} (W/K)	T_{max} (°C) (T_c = 35 °C)
1	5	50	0.54	50	300	15	22.06	0.54	46.91
2	7.5	50	0.54	50	300	15	15.23	0.35	40.33
3	10	50	0.54	50	300	15	12.46	0.285	38.55
4	10	150	0.35	50	300	15	9.39	0.21	36.97
5	10	50	0.54	75	300	15	18.31	0.31	40.68
6	10	50	0.54	100	300	15	23.76	0.34	43.08

Table 3
Predicted maximum heat transfer of TVCs with optimized fin diameter and porosity under both the capillary limit and the allowable maximum temperature limit (70 °C).

Radius (mm)	d_f (μm)	ε	h_w (μm)	h (μm)	Q_{max} (W)	R_{th} (W/K)	T_{max} (°C) (T_c = 35 °C)
1.6	60	0.66	41.6	416	11.75	2.98	Limited by 70 °C
4	150	0.58	41.6	416	62.12	0.56	Limited by 70 °C
8	70	0.80	41.6	416	45.85	0.41	53.72
10	70	0.80	41.6	416	42.44	0.35	49.99
15	80	0.80	41.6	416	38.14	0.30	46.40

Although not the most significant effect, Fig. 7 (a) shows that the maximum temperature decreases as the fin diameter increases. Also, as shown in Fig. 7 (b), the thermal resistance of TVCs decreases as the fin diameter increases. This implies that the porosity, which only depends on the fin diameter under the fixed separation distance between the fins, affects the effective thermal conductivity of the wick structures and its thermal resistance. So, as the fin diameter is increased the porosity is decreased. Therefore, the maximum temperature and the total thermal resistance both decrease because the effective thermal conductivity increases.

4.2.3. Effect of wick height on the maximum temperature and the thermal resistance

Cases 3, 5 and 6 show the effect of wick height on the maximum temperature and the thermal resistance. As shown in Fig. 8(a), larger maximum temperatures are associated with taller wick fin heights. For all other geometry parameters being fixed, Fig. 8(b) shows that taller wick fin heights induce larger thermal resistances. Consequently, low wick fin heights are desirable to avoid exceeding the maximum allowable temperature of electronic components.

5. Conclusion

The thermal characteristics of disk-shaped silicon-wafer-based TVCs (Thin Vapor Chambers) heat pipes were analytically and experimentally investigated using DI-water as working fluids. Analytical models for the maximum heat transfer rate of the TVC were developed using both the capillary limit and the allowable maximum temperature limit. Six silicon wafer-based TVCs were manufactured using DRIE (deep reactive ion etching) and anodic bonding. The measurements of the maximum temperature and the thermal resistances of the TVC showed the effect of TVC radius, the fin diameter, and the wick fin height on the TVC performance. A laser heat source and an IR camera were used to eliminate the effect of contact thermal resistance and to observe the behavior of burn-out phenomena in silicon wafer-based TVCs. Based on the results, it was shown that the analytical model for maximum heat transfer rate predicts the experimental data to within ±10%.

Conflict of interest

The authors declare that there are no conflicts of interest.

Acknowledgment

This work was supported by a grant from the Space Core Technology Development Program of National Research Foundation of Korea (NRF), funded by the Korean government (MSIP) (NRF–2015M1A3A3A02014936). The authors thank the following for their constructive criticism of the first draft of the manuscript: H. Skye from NIST, and K.H. Do from Korea Institute of Machinery and Materials.

References

[1] S. Krishnaswamy, P. Jain, M. Saeidi, A. Kulkarni, A. Adhiya, J. Harvest, Fast and accurate thermal analysis of smartphone with dynamic power management using reduced order modeling, in: 16th IEEE ITHERM Conference, 2017, pp. 276–286.
[2] G. Patankar, J.A. Weibel, S.V. Garimella, Patterning the condenser-side wick in ultra-thin vapor chamber heat spreaders to improve skin temperature uniformity of mobile devices, Int. J. Heat Mass Transf. 101 (2016) 927–936.
[3] S. Launay, V. Sartre, M. Lallemand, Experimental study on silicon micro-heat pipe arrays, Appl. Therm. Eng. 24 (2004) 233–243.
[4] J.-C. Wang, R.-T. Wang, T.-L. Chang, D.-S. Hwang, Development of 30 watt high-power LEDs vapor chamber-based plate, Int. J. Heat Mass Transf. 53 (2010) 3990–4001.
[5] Y.S. Ju, M. Kaviany, Y. Nam, S. Sharratt, G.S. Hwang, I. Catton, E. Fleming, P. Dussinger, Planar vapor chamber with hybrid evaporator wicks for the thermal management of high-heat-flux and high-power optoelectronic devices, Int. J. Heat Mass Transf. 60 (2013) 163–169.
[6] W. Liu, Y. Peng, T. Luo, Y. Luo, K. Huang, The performance of the vapor chamber based on the plant leaf, Int. J. Heat Mass Transf. 98 (2016) 746–757.
[7] G. Patankar, J.A. Weibel, S.V. Garimella, Working-fluid selection for minimized thermal resistance in ultra-thin vapor chamber, Int. J. Heat Mass Transf. 106 (2017) 648–654.
[8] L. Lv, J. Li, Managing high heat flux up to 500 W/cm^2 through an ultra-thin flat heat pipe with superhydrophilic wick, Appl. Therm. Eng. 122 (2017) 593–600.
[9] H. Aoki, N. Shioya, M. Ikeda, Y. Kimura, Development of ultra thin plate-type heat pipe with less than 1 mm thickness, in: 26th Annual IEEE Semiconductor Thermal Measurement and Management Symposium (SEMI-THERM), CA, Santa Clara, 2010, pp. 217–222.
[10] R. Lewis, S. Xu, L.-A. Liew, C. Coolidge, R. Yang, Y.-C. Lee, Thin flexible thermal ground planes: fabrication and scaling characterization, J. Microelectromech. Syst. 24 (2015) 2040–2048.
[11] S.-C. Wong, K.-C. Hsieh, J.-D. Wu, W.-L. Han, A novel vapor chamber and its performance, Int. J. Heat Mass Transf. 53 (2010) 2377–2384.
[12] M. Wei, S. Somasundaram, Optimization of biporous micropillar array for enhanced heat transfer performance, in: Proc. IMECE (2015), Texas, Houston, IMECE2015-52651.
[13] K. Vafai, N. Zhu, W. Wang, Analysis of asymmetric disk shaped and flat-plate heat pipes, ASME Trans. J. Heat Transf. 177 (1995) 209–218.
[14] K.H. Kim, S.-H. Lee, H.J. Kim, S.P. Jang, Discussion: "Analysis of asymmetric disk-shaped and flat-plate heat pipes", ASME Trans. J. Heat Transf. 136 (2014) 115501–115502.
[15] M. Kaviany, Principles of Heat Transfer in Porous Media, 2nd ed., Springer-Verlag, New York, 1991, p. 43.
[16] S.J. Kim, J.K. Seo, K.H. Do, Analytical and experimental investigation on the operational characteristics and the thermal optimization of a miniature heat pipe with a grooved wick structure, Int. J. Heat Mass Transf. 46 (2003) 2051–2063.
[17] R.R. Thomas, F.B. Kaufman, J.T. Kirleis, R.A. Belsky, Wettability of polished silicon oxide surfaces, J. Electrochem. 143 (1996) 643–648.
[18] K.-S. Chen, A.A. Ayon, X. Zhang, S.M. Spearing, Effect of process parameters on the surface morphology and mechanical performance of silicon structures after deep reactive ion etching (DRIE), J. Microelectromech. Syst. 11 (2002) 264–275.
[19] F.P. Incropera, D.P. Dewitt, Introduction to heat transfer, 6th ed., John Whey & Sons, 2008.
[20] A. Faghri, Heat pipe science and technology, 1995.
[21] S.W. Chi, Heat Pipe Theory and Practice, Hemisph. Publ. Corp., McGraw-Hill B. Co., Washington, D.C., New York, 1976, 256P.
[22] F. Lefèvre, R. Rullière, G. Pandraud, M. Lallemand, Prediction of the temperature field in flat plate heat pipes with micro-grooves - experimental validation, Int. J. Heat Mass Transf. 51 (2008) 4083–4094.
[23] E.H. Klaassen et al., Silicon fusion bonding and deep reactive ion etching: a new technology for microstructures, Sensors Actuat. A Phys. 52 (1996) 132–139.
[24] H.T. Lim, S.H. Kim, H.D. Im, K.H. Oh, S.H. Jeong, Fabrication and evaluation of a copper flat micro heat pipe working under adverse-gravity orientation, J. Micromech. Microeng. 18 (2008) 105013.
[25] V.M. Aroutiounian, K. Martirosyan, P. Soukiassian, Low reflectance of diamond-like carbon/porous silicon double layer antireflection coating for silicon solar cells, J. Phys. D. Appl. Phys. 37 (2004) L25–L28.